The Astrophysical Journal Letters, 881:L25 (8pp), 2019 August 10 https://doi.org/10.3847/2041-8213/ab365b

High-resolution Spectroscopic Imaging of Counter-streaming Motions in Solar Active Region Magnetic Loops

Xu Yang[1], Wenda Cao[1,2], Haisheng Ji[3,4], Parida Hashim[5,6], and Jinhua Shen[5]
[1] Center for Solar-Terrestrial Research, New Jersey Institute of Technology, 323 Martin Luther King Boulevard, Newark, NJ 07102, USA; xy88@njit.edu
[2] Big Bear Solar Observatory, New Jersey Institute of Technology, Big Bear City, CA 92314, USA
[3] Key Laboratory for Dark Matter and Space Science, Purple Mountain Observatory, CAS, Nanjing, 210008, People's Republic of China
[4] China Three Gorges University, Yichang, 443002, People's Republic of China
[5] Xinjiang Astronomical Observatory, CAS, Urumqi, 830011, People's Republic of China
[6] University of Chinese Academy of Sciences, Beijing, 100049, People's Republic of China
Received 2019 May 7; revised 2019 July 24; accepted 2019 July 24; published 2019 August 13

Abstract

We carried out high-resolution spectroscopic imaging in He I 10830 Å and H_α for a set of active region (NOAA 12569) magnetic loops of different sizes (classified into short and long loops) with the Goode Solar Telescope at the Big Bear Solar Observatory on 2016 July 18. The long loops take the form of an chromospheric arch filament system, yet their extreme ultraviolet (EUV) counterparts are observed by the Atmospheric Imaging Assembly on board the *Solar Dynamics Observatory*. Animations of blue- and red-wing images give counter-streaming motions; i.e., chromospheric absorption features in blue- and red-wing images move in opposite directions at different strands. The moving pattern is detected with the local correlation tracking method and confirmed by Doppler shifts. We speculate that, combined with the results of wavelet analysis that gives obvious 4 minute oscillation along trailing polarity, counter-streaming motions for short loops could be powered by p-mode leakage. However, for counter-streaming motions in long loops, we show that unidirectional mass flows in two opposite directions are accompanied with simultaneous weak EUV brightenings. Heating processes, probably by magnetic reconnection at footpoints, may have occurred. In addition, plasma flows along the magnetic loops, tracked with absorption features in He I 10830 Å, are found to be ejected from and drained out into inter-granule lane areas at different ends of the loop system.

Key words: Sun: chromosphere – Sun: corona – Sun: granulation – Sun: photosphere

Supporting material: animations

1. Introduction

The highly magnetized solar upper atmosphere consists of numerous discrete fine-scale magnetic loops, the brightness of which comes from confined plasma of different temperatures. More and more observations and models show that the magnetic loops are far from hydrostatic. Consequently, the motions of plasma along the loops are very important for mass transfer and energy exchange between the upper and lower solar atmosphere, which is a key physical process for understanding the problem of coronal heating (Martínez-Sykora et al. 2011). Tremendous advances in this topic have been achieved since the space age and high-resolution era (see Aschwanden et al. 2000; Reale 2014 and references therein). Generally speaking, we can conclude that there are three kinds of flowing patterns in coronal loops: upward filling (e.g., Sakao et al. 2007; Hara et al. 2008; He et al. 2010; Pontieu & McIntosh 2010; Tian et al. 2011a, 2011b; Tian 2017), downward draining (e.g., Pneuman & Kopp 1978; Winebarger et al. 2013), and siphon flows (e.g., Teriaca et al. 2004). All of the results were obtained via measurements of intensity perturbation in images and, especially, Doppler shifts observed by space-based as well as ground-based instruments.

Many observations show that the Doppler shifts are temperature-dependent, bifurcating toward low temperature (redshifts) and high temperature range (blueshifts), respectively (Dadashi et al. 2011). The transition from red to blue appears to occur at about 0.5–1 MK (Dadashi et al. 2012; Tripathi et al. 2012). More importantly, they appear to be "co-spatial" (Zanna 2008; Kamio et al. 2011; Warren et al. 2011). For example, McIntosh et al. (2012) reported weakly emitting upward propagating disturbances in both hot and cool emission with apparent speeds of 50–150 $\mathrm{km\,s^{-1}}$, as well as co-spatial persistent slower draining downflows ($\sim$10 $\mathrm{km\,s^{-1}}$) seen in cool emission; they termed the phenomenon "contraflow" (or counter-streaming flows). The counter-streaming flows are important signature of mass and energy cycling between the chromosphere and the corona (e.g., McIntosh & Pontieu 2009; Pontieu et al. 2011). In the chromosphere, magnetic loops often take the form of arch filament system (AFSs; Bruzek 1967). An AFS is usually formed at an emerging flux region (EFR), where magnetic flux is transferred to the solar surface by magnetic buoyancy. Generally, a rising AFS traps photospheric material that drains down along both loop legs as the arch rises (Bruzek 1969). Meanwhile, magnetic reconnections between the footpoints of AFSs and pre-existing ambient fields with opposite polarities can cause magnetic energy to be released, and facilitate the field-aligned movement of extreme ultraviolet (EUV) brightenings (Tarr et al. 2014).

The dynamics of solar filaments (e.g., Parenti & Vial 2013) and chromospheric loops (e.g., Ji et al. 2012) have been studied in H_α, He I 10830 Å and EUV observations through the analysis of the paths of absorption features and Doppler shift. Tracing the features of time-sequence images and analyzing spectral line profiles reveal two complementary components: plane-of-sky velocity and the line-of-sight (LOS) motion of mass flows. Counter-streaming flows on the Sun were first discovered in filaments (Zirker et al. 1998; Shen et al. 2015).

Because of insufficient spatial resolution, we were unable to separate the superimposed upflows and downflows. With the application of high-spatiotemporal-resolution observations, researchers can study low atmospheric structures with an unprecedented level of detail. Zou et al. (2016) analyzed an active region (AR) filament and indicated that the filament is supported by sheared arcades without magnetic dips, and that the counter-streaming motion is due to unidirectional flows with alternative directions, while Wang et al. (2018) reported that the counter-streaming motion of an AR filament above a sunspot light bridge is due to physical mass motion along threads. With the advent of large-aperture telescopes, pinning down the origin of these chromospheric flows in the photosphere will help us to understand not only the nature of counter-streaming flows in chromosphere, but also the problem of coronal heating. A previous study has shown the unique role that high-resolution He I 10830 Å imaging with a large-aperture solar ground-based telescope plays in precisely locating the roots of coronal loops in the photosphere (Ji et al. 2012). For AR loops, they found that upward mass and energy flows of ultrafine channels are rooted in inter-granule lanes. With the same set of data, energy sources originating from inter-granule lanes heating solar upper atmosphere were revealed in solar quiet regions (Hong et al. 2017).

With the aim to further investigate the mass and energy flows in coronal loops, we carried out high-resolution spectroscopic imaging in He I 10830 Å for an AR with the 1.6 m aperture Goode Solar Telescope at Big Bear Solar Observatory (GST at BBSO; Goode et al. 2010). Simultaneous high-resolution photospheric filtergrams in TiO 7057 Å and chromospheric spectroscopic images in H_α were acquired with GST. In this Letter, we present the first observations of counter-streaming motions of arcade fibrils in an AR obtained with the He I 10830 Å spectroscopy. Observations and results are given in Sections 2 and 3, followed by a summary in Section 4.

2. Observations

On 2016 July 18, we observed NOAA AR 12569 at N16 E35 (the GST field of view (FOV) center was at $x = -518''$, $y = 206''$, $\mu \equiv \cos\theta = 0.59$) using the Near Infra-Red Imaging Spectropolarimeter (NIRIS; Ahn et al. 2016), the Visible Imaging Spectrometer (VIS; Cao et al. 2010a), and the Broadband Filter Imager (BFI; Cao et al. 2010b) with the aid of adaptive optics (AO) system AO-308 (Shumko et al. 2014). NIRIS uses a single Fabry–Pérot etalon to provide an $85''$ round FOV imaged on a Teledyne camera, which is a 2k $\times$ 2k HgCdTe, closed-cycle helium-cooled infrared (IR) array. NIRIS offers an imaging spectroscopic observations in He I 10830 Å, with a bandpass of 0.05 Å and an image scale of $0\farcs063$/pixel. Typically, NIRIS takes about 3 s for an acquisition of a burst of frames in one certain wavelength point to achieve high temporal resolution data set, the spectroscopy observations were performed at line center and ±0.2, ±0.4, ±0.6, ±0.8 Å of the He I 10830 Å line red component. BFI provides high-contrast imaging on the photosphere in the TiO molecular bands in 7057 Å. It has a cadence of 15 s and an FOV of $70'' \times 70''$ with an image scale of $0\farcs034$/pixel. VIS is based on a visible Fabry–Pérot interferometer to provide imaging spectroscopy in the H_α. The spectroscopy observations were performed at line center and ±0.4, ±0.8, ±1.0 Å of the H_α line. VIS takes 3 s to acquire a burst of frames and its temporal cadence was set to 30 s (with a 9 s delay between each full wavelength scan) to obtain seven wavelengths of data over a $74'' \times 68''$ FOV at $0\farcs029$/pixel. The AR was observed from 16:35:51 UT to 22:37:39 UT, while the data between 20:20:55 UT and 20:45:25 UT are selected for this study. Corresponding ultraviolet (UV) and EUV observations are provided by AIA (Lemen et al. 2011) on board *SDO*.

AO-308 utilizes a wavefront sensor of 308 sub-apertures across the telescope pupil. During most of the observing time, the high-order AO-308 helps GST acquire the diffraction limit of the telescope. Photospheric images of TiO and chromospheric spectroscopic imaging in the Hα, He I 10830 Å lines were flat-fielded and then speckle reconstructed to further minimize the residual aberrations using the Kiepenheuer-Institut Speckle Interferometry Package KISIP7 code (Wöger et al. 2008).

Data sets of different wavelengths were spatially co-aligned for the time of 2016 July 18 20:21 UT by taking a Helioseismic and Magnetic Imager (HMI)/*SDO* (Schou et al. 2011) continuum image as a reference. Then each data set was reduced by performing alignment to that time. Utilizing the sub-pixel shift method, we acquired the well-aligned data sets with an alignment accuracy that is better than $0\farcs03$.

3. Results

Figure 1 provides snapshots of overall observations for AR NOAA 12569. The map for the LOS magnetic field observed by HMI in panel (f) gives the overall magnetic structure of the AR. The AR contains a negative leading polarity and a positive trailing polarity, between which a bipolar magnetic flux emerged, forming a typical quadrupole magnetic configuration. The FOV of GST observations in Hα and He I 10830 Å is marked by a black box in the panel, with two sample GST images given in panels (a) and (b). Panels (c)–(e) show corresponding AIA/*SDO* observations in 304, 171, and 1600 Å with the same FOV as the black box. Note that around the trailing sunspot is a diffusive plage area. The plage area for negative polarity of the emerging flux forms a narrow strip (panel e).

In the FOV, roughly two kinds of loops can be seen from space and ground observations: higher fan-like loops prominently in 171 Å images and low-lying arcade loops in 10830 Å. Furthermore, as displayed by the He I 10830 Å image, we can divide the low-lying arcade loops in the FOV into two sets according to their different morphology and connectivity. They have different lengths and curvature, all starting from the trailing polarity (or the diffusive plage region) of the AR. Short and highly curved loops, which are located in the upper part of area 2, get into nearby network polarity while long and more straight loops connect with the adjacent polarity of the emerging flux. Notably, in H_α images, the long loops are actually an AFS. However, the AFS is not an emerging flux and it has weak EUV emissions at all AIA wavelengths, showing that it is slightly heated. Meanwhile, Figure 1(a) gives the counterpart of an AFS in He I 10830 Å. In the coming analysis, we will refer to them as short loops and long loops, respectively.

Comparing animations of blue-wing and red-wing images of either He I 10830 Å or Hα immediately demonstrates obvious counter-streaming motion patterns in the low-lying arcade loops, teeming in the northwest quarter of Figure 1(a) (the area in the white box, see the animation associated with Figure 2).

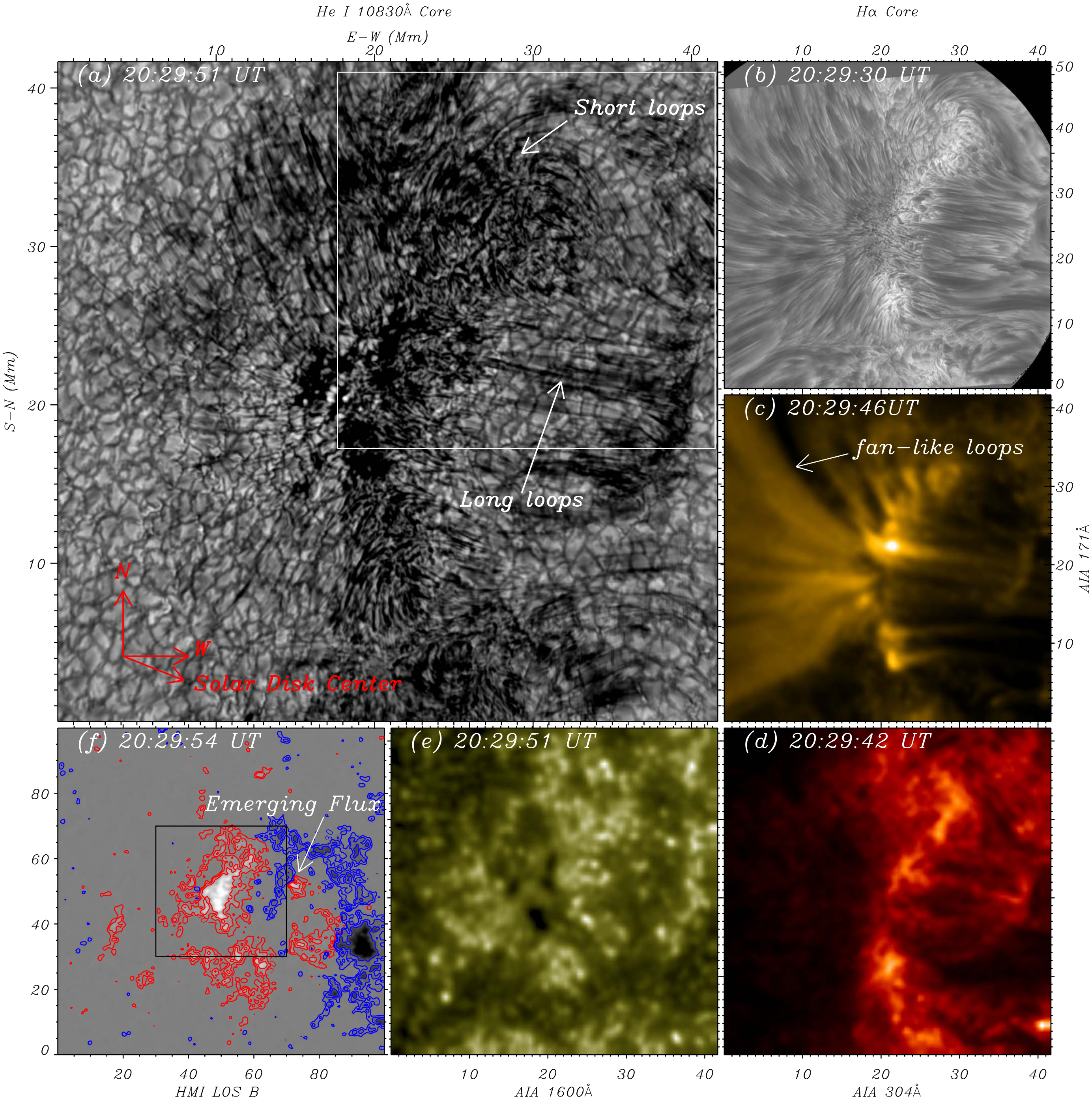

Figure 1. Overview of the AR NOAA 12569 observed on 2016 July 18. Panels (a) and (b), with the same FOV, display snapshots of high-resolution spectroheliograms in He I 10830 Å and H_α line center. Simultaneous observations, with the same FOV, by AIA on board *SDO* are given in panels (c)–(e), which in turn are maps of 171, 304, and 1600 Å. Panel (f) gives the map of the LOS magnetic field observed by HMI on board *SDO* with a larger FOV, in order to give an overall magnetic structure of the AR. Red/blue contours depict the magnetic field in the range of $\pm 30 \sim 300$ Gauss. Note that the contours share a similar configuration with brightened network areas in 1600 Å in panel (e).

We constructed flow maps with the local correlation tracking (LCT; November & Simon 1988) method to show the observed counter-streaming motions (Figure 2).

The mass flow directions inside the loop fibrils are opposite between blue-wing and red-wing images. The blue-wing images illustrate flows moving in a clockwise (CW) pattern in the region of short loops (deep blue arrows) and a westward pattern in the long loops (light blue arrows). Meanwhile, the red-wing images demonstrate an opposite flow pattern (see the Figure 2 animation). High-resolution images unambiguously show that the counter-streaming flows occur along alternative loops. Considering the AR's location and viewing angle from the Earth, the observations show that the counter-streaming flows might be due to unidirectional mass flows driven by material injection at loop footpoints. We can exclude the possibility of downward streaming at two different sides of the arcade loops, because it cannot produce the flow pattern shown in Figure 2.

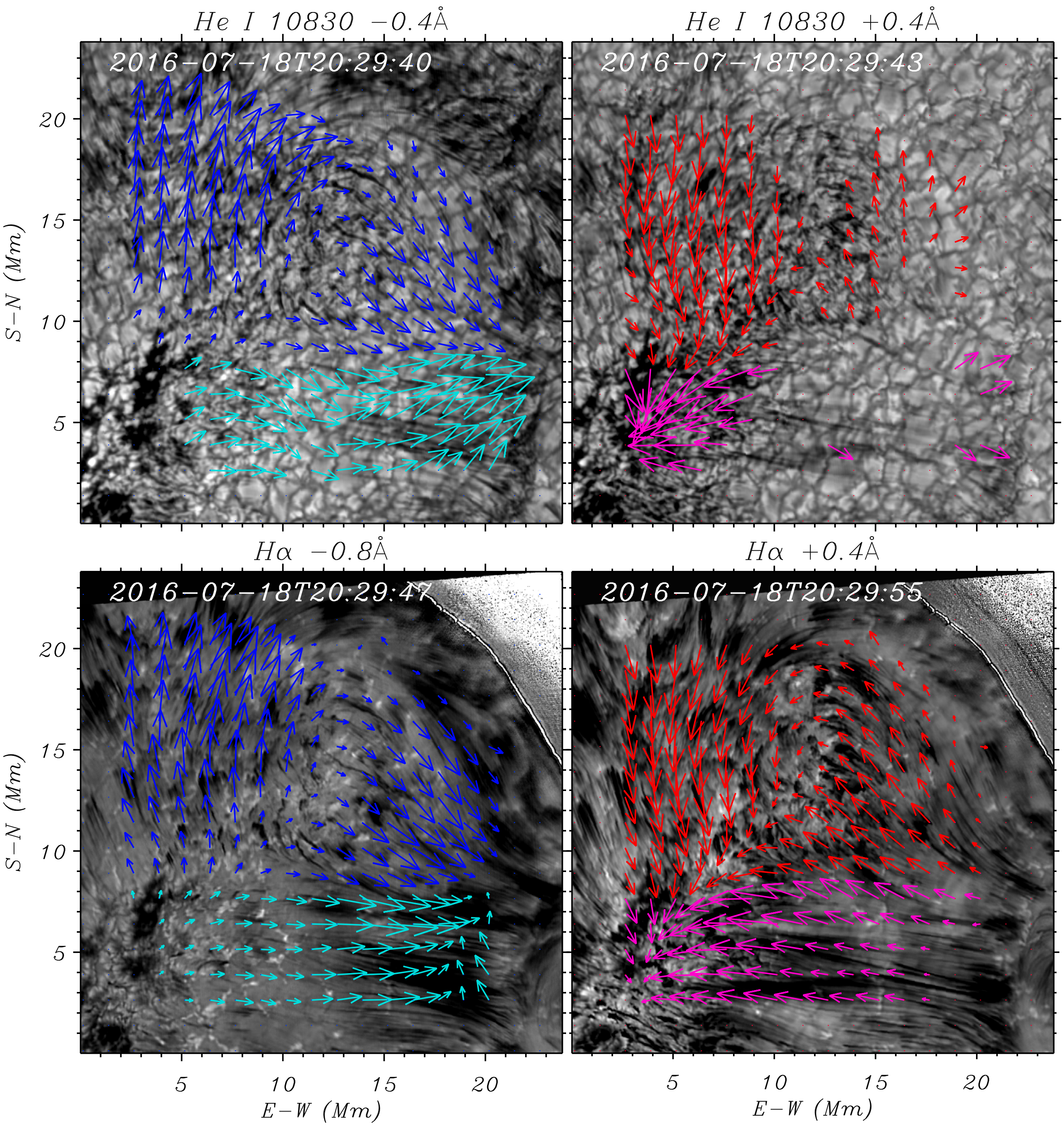

Figure 2. Flow maps created with He I 10830 and H_α off-band observations. Top panels: mass flow maps constructed with He I 10830 ± 0.4 Å data sets. Bottom panels: mass flow maps constructed with H_α −0.8 Å and +0.4 Å data sets. The flow maps are derived with the LCT method. The animation illustrates the counter-streaming patterns in the He I 10830 and H_α off-band observations. The animation also shows the AIA 304 Å (top-right panel) and AIA 171 Å (bottom-right panel) sequence. All of the panels in the animation begin around 20:20 UT and end after 20:44 UT. The video duration is 8 s.

(An animation of this figure is available.)

To illustrate the counter-streaming motion patterns, we select two loops as shown in Figure 3. The material in long loop 1 flows toward the solar limb (eastward) and only contains a red-wing absorption signal, while long loop 2 demonstrates an opposite phenomenon: it flows westward and only contains a blue-wing absorption signal. Time–distance diagrams for both loops are given in Figure 4; the apparent flow velocities are found to be 16–25 km s^{-1} for westward motion, and around 15 km s^{-1} for eastward motion. In particular, simultaneous and co-spatial brightenings can be found and they give clear evidence of warm ($\sim 10^5$ K) plasma flows in the same direction, suggesting heating processes.

To confirm the flow patterns inside of these loops, we carried out line fitting with a Gaussian profile as an approximation to He I 10830 Å lines. We performed velocity calibration by setting the line shift averaged over a quiet region near the solar disk center to zero. Doppler velocity is thus obtained from line center shifting and the map is provided in panel (c1) of Figure 3. The same loops (loop 1 and 2) are indicated by the colored double solid lines. The Doppler velocity along the two

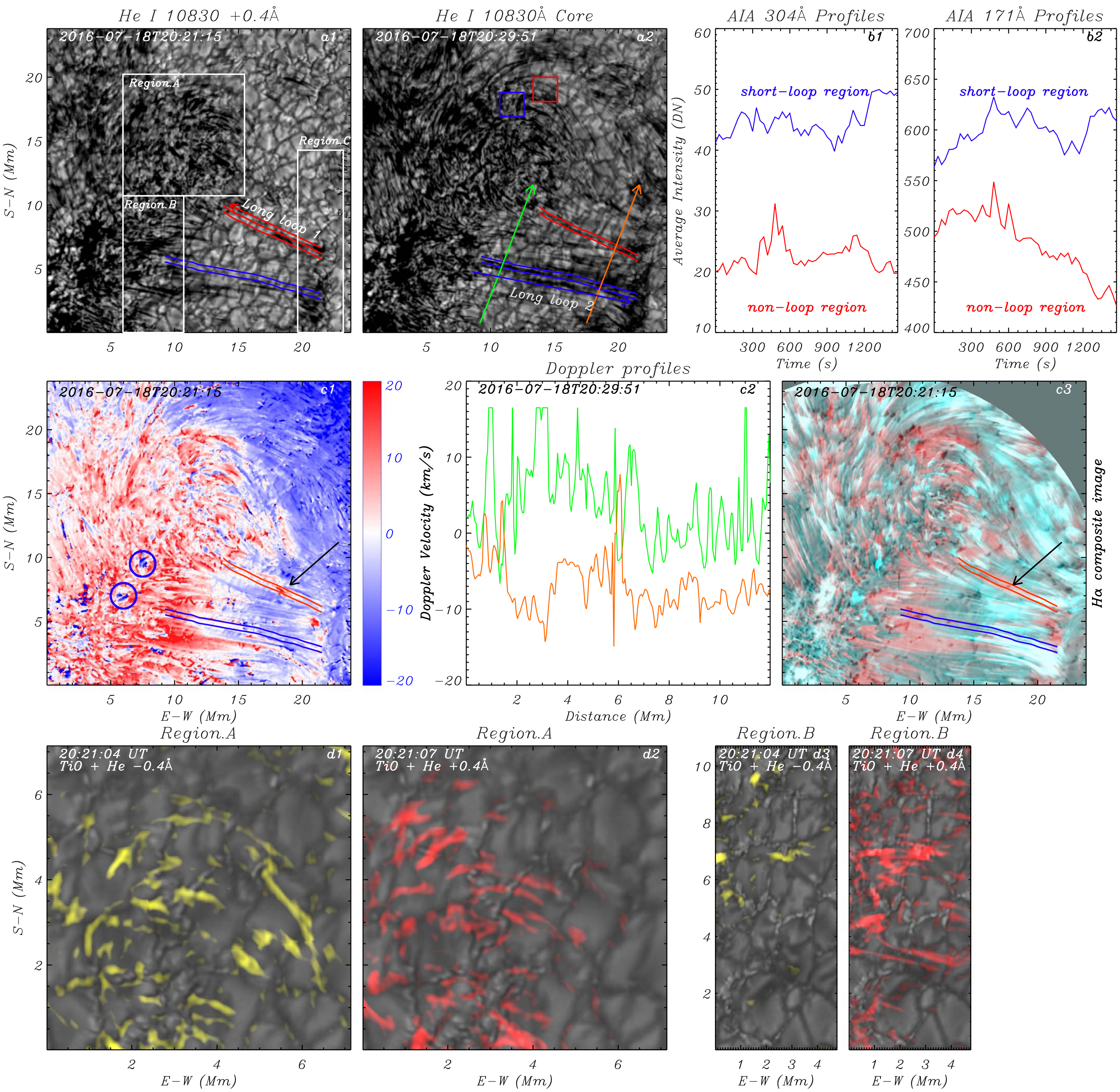

Figure 3. Panel (a1) and (a2): sample He I 10830 Å images overlaid with region information for other panels and Figure 4. The double solid lines in different colors mark each selected long loop, with the nearby arrow indicating the flow directions inside the loop. Panel (b1) and (b2): blue light curves are for averaged intensities in 171 and 304 Å over the area of short loops (i.e., with He I 10830 Å absorption, blue box in the top-left panel) and red light curves are over the area of little He I 10830 Å absorption (red box in the top-left panel). Doppler velocity maps created with He I 10830 Å spectroscopy data. The black arrows indicate the redshifted mass flow inside the long loop 1. The blue circles indicate clusters of blueshifted flows in and around the Region B. Panel (c2): Doppler velocity profiles along the two slits (green and orange arrow) in panel (a2). The blue circles indicate clusters of blueshifted flows in Region B. Panel (c3): a composite image created with H_α off-band images, showing the different loop positions. Panel (d1)–(d4): composite images for Region A and B. The background is TiO and the yellow/red color represents the absorption features in He 10830 −0.4 Å and +0.4 Å, respectively. Region A contains short loops, while long loops are mainly rooted in the region B and C. An animation of panels (c1) and (c3) is available. Both animations cover 20:20 UT to 20:44 UT with 30 s cadence. The durations of the videos is 8 s.

(An animation of this figure is available.)

loops basically confirms the conclusions given above. The Doppler velocity can be as high as $\pm 20\,\mathrm{km\,s^{-1}}$ for redshifted and blueshifted components. A composite image made of H_α blue-wing and red-wing images is given in panel (c3) of Figure 3. The unidirectional motion in loop 1 and 2 is again confirmed.

For the long loops, absorption features in both He I 10830 Å and H_α in the two footpoint regions are strongly imbalanced. For the left footpoint area (region B in Figure 3), we see more absorption features in red-wing images. Meanwhile, more absorption features can be seen near the right footpoint area (region C) in blue-wing images. We speculate that material for

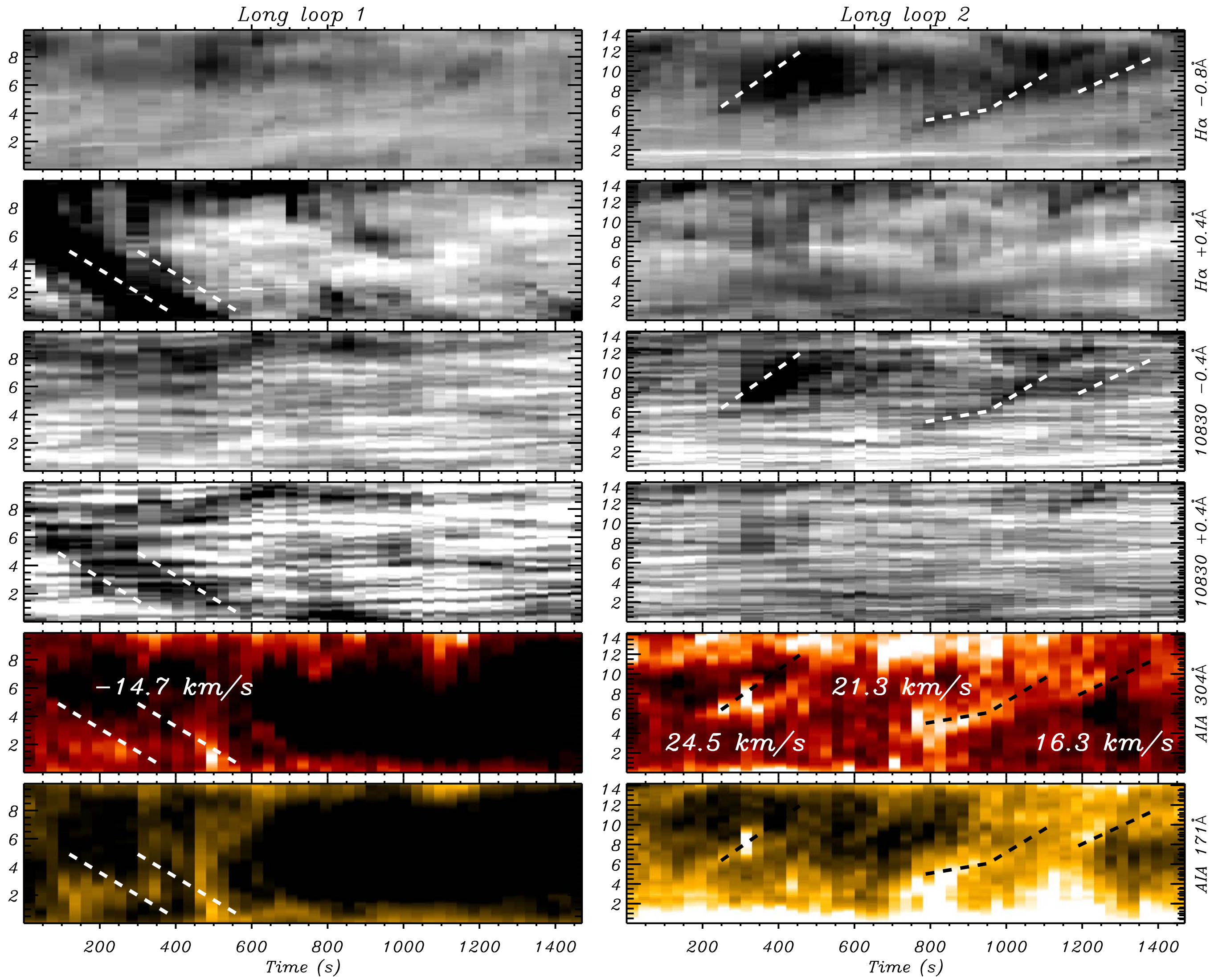

Figure 4. Time–distance diagrams in H_α −0.8 Å and +0.4 Å, He I 10830 ± 0.4 Å, AIA 304 and 171 Å for the cutting strips along the long loop 1 and long loop 2. Note that the red-wing absorption features in He I 10830 Å and H_α move eastward along the long loop 1, as indicated by the arrow in the Figure 3(a1). The mass flow inside the long loop 2 is also unidirectional and only contains blue-wing absorption features.

drainage at one side comes from injection at the other side footpoints. As stated in the Introduction, material injection is usually hot and, thus, will not be observed with the line from neutral helium atoms. Material ejected from one footpoint of a strand is cooling down and slowing down when it arrive at the other footpoint. The pattern seen in the Doppler map is reflecting downward drainage. However, we see that the drainage is not like that observed in a rising AFS.

Furthermore, the dominated line-shift pattern at the two sides contains some oppositely line-shifted components. Panel (c2) of Figure 3 gives the distributions of Doppler velocity along two parallel lines (green and orange lines in panel (c2)) right across the long loops near the two footpoint regions. Occasional opposite flow directions are evident, especially alone the green line, and demonstrate the occasional ejection of cool material.

On the other hand, the short loops exhibit repeating surge-like motions in the line core with slower speeds (less than $5\,\mathrm{km\,s^{-1}}$), and their response in the higher atmosphere is not obvious. The space scale of short loops is normally around $2 \sim 3$ Mm, which is only $5 \sim 7$ pixels in the AIA image. Thus, it is hard to generate time–distance diagrams for the short loops. However, the light curve diagrams (Figure 3, top-right panels) reveal the correspondence between He I 10830 Å absorption features and EUV emissions. We compared the average intensities in a region containing abundant short loops (short-loop region, red box) and a nearby region containing very little He I 10830 absorption (blue box). The EUV emission above the short loop is significantly higher than the region without He I 10830 Å loops.

The He I 10830 Å is optically thin in most parts of the solar chromosphere and information from solar photosphere can be obtained from the He I 10830 Å spectroheliogram. Thus, alignment between the photospheric and chromospheric images can be carried out at precision of an unprecedented level, being up to less than 0.2 arcsec. This advantage has led to a finding that He I 10830 Å blue-wing absorption features are rooted in the inter-granule lanes (Ji et al. 2012; Hong et al. 2017). In a similar way, we make composite RGB images by overlapping absorption features of both the blue wing and the red wing in simultaneous TiO images. The lower-left two panels of Figure 3 give the results for the region of short loops, where

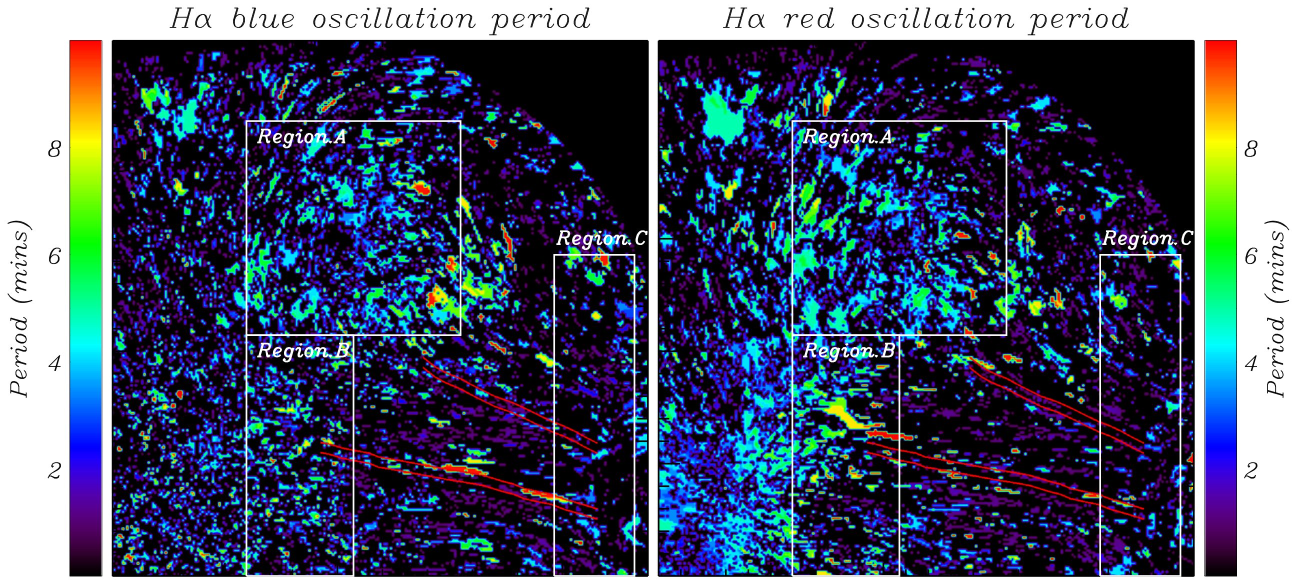

Figure 5. Maps for the dominating oscillation period obtained from wavelet analysis with H_α line wing images. Regions A, B, and C are the same as those depicted in Figure 3.

there are abundant 10830 Å absorption features in both the blue wing and the red wing. We see that the 10830 Å absorption features, either in the blue wing or the red wing, are mostly located around the area of inter-granule lanes. Only region B is well covered by the FOV of TiO images. Composite images for this area confirmed the above results; i.e., we see that material flows into and out of the area of inter-granule lanes. This shows us that footpoints of magnetic loops are rooted in inter-granule lanes.

From the animations, we can see that absorption features exhibit a kind of periodic behavior, especially in the diffusive plage area. We carried out "Wavelet Analysis for Images" (Torrence & Compo 1998) of Hα red and blue wings, with oscillation period maps being given is Figure 5. A strong oscillation signature with a period of ∼4 minutes dominates the diffusive plage area where the short loops take their roots, which shows the possible leakage of photospheric p-mode oscillation. However, in the strip plage area, oscillation signature is scarce. Mass flows inside of the long loops, and co-spatial EUV brightenings show an impulsive nature when they flow out of and into the footpoint area. Even though some strands give oscillation periods peaking around $9 \sim 10$ minutes, they may actually reflect the time interval between the mass flow tracks obtained in Figure 4. We speculate that the flows in the long loops are driven by magnetic reconnection.

4. Summary

With GST at BBSO, we carried out high-resolution spectroscopic imaging in helium I 10830 Å for upper chromosphere loops, aiming to understand mass and energy flows in the interface region from below. Studies of AFS based on the He I 10830 Å triplet reported slow upflows of 1.5–20 km s^{-1} in the center of the arches (Solanki et al. 2003; Xu et al. 2010) and downflows of 15–90 km s^{-1} at the footpoints (Lagg et al. 2006; Manrique et al. 2018). In our study, blue-wing and red-wing images in He I 10830 Å and H_α give apparent side-by-side counter-streaming flows inside AR arcade loops with an unprecedented high-spatial resolution. Simultaneous auxiliary yet indispensable spectroscopic imaging in H_α and broadband imaging in TiO 7057 Å were obtained. Blue-wing and red-wing images in He I 10830 Å and H_α give apparent side-by-side counter-streaming flows inside AR arcade loops with an unprecedented high-spatial resolution. Considering the location of the AR on the Sun and the loops' low height, the counter-streaming motions actually reflect motions along two opposite directions that are nearly parallel to the solar surface. Our observational findings show that the counter-streaming motions are due to unidirectional mass flows along alternative loop strands.

The magnetic loops where counter-streaming flows connect two plage areas (network regions) formed around the trailing polarity of the AR and a nearby emerging polarity. In spectroscopic images in He I 10830 Å, the flows take the form of moving absorption features. A precise alignment between 10830 Å images and corresponding photospheric images taken in TiO 7057 Å allow us to find that plasma flows are pumped up from and drained down to the inter-granule lanes. While the phenomena of plasma flowing out of inter-granule lanes along ultrafine channels has being reported (Ji et al. 2012), the results of this Letter not only confirm the results but also show that plasma flows into inter-granule lanes along ultrafine channels. This indicates that each strand of a magnetic loop is ultimately rooted in inter-granule lanes.

The moving absorption features in He I 10830 Å along long distances (long loops in this Letter) are apparently accompanied by co-spatial EUV emissions in AIA 304 and 171 Å images, and the moving features are impulsive. No co-spatial EUV emissions are found during short-range surge-like ejections of absorption features (short loops in this Letter). However, average EUV emission over these short absorption features is much higher than that of the rest of regions. Therefore, these results confirm that heating sources of TR are located in inter-granule lanes.

Wavelet analysis shows that the oscillation power inside of these short loops peaks around 4 minutes, indicating the possible role of p-mode in pumping out short-range plasma ejections. However, there is no evidence that the unidirectional mass flowing inside of the long loops is also modulated by p-modes. We speculate that magnetic magnetic reconnection or cancellation may play a major role in powering the long-range flows. Further study with high-resolution magnetograms may reveal the role of fine-scale magnetic network activities in powering the counter-streaming mass flows.

We especially thank the anonymous referee for constructive comments that helped to improve this Letter.

We thank the BBSO observing staff for their assistance during data acquisition and AIA/*SDO* team for providing the space data. Ji, Hashim and Shen are supported by CNFC 11790300, 11729301, and 11773061. The BBSO operation is supported by US NSF AGS-1821294, New Jersey Institute of Technology and the Korea Astronomy and Space Science Institute and Seoul National University.

ORCID iDs

Xu Yang https://orcid.org/0000-0002-3238-0779
Wenda Cao https://orcid.org/0000-0003-2427-6047
Jinhua Shen https://orcid.org/0000-0003-3382-7795

References

Ahn, K., Cao, W., Shumko, S., & Chae, J. 2016, AAS/SPD meeting, 47, 2.07
Aschwanden, M. J., Nightingale, R. W., & Alexander, D. 2000, ApJ, 541, 1059
Bruzek, A. 1967, SoPh, 2, 451
Bruzek, A. 1969, SoPh, 8, 29
Cao, W., Gorceix, N., Coulter, R., et al. 2010a, AN, 331, 636
Cao, W., Gorceix, N., Coulter, R., Coulter, A., & Goode, P. R. 2010b, Proc. SPIE, 7733, 773330
Dadashi, N., Teriaca, L., & Solanki, S. K. 2011, A&A, 534, A90
Dadashi, N., Teriaca, L., Tripathi, D., Solanki, S. K., & Wiegelmann, T. 2012, A&A, 548, A115
Goode, P. R., Yurchyshyn, V., Cao, W., et al. 2010, ApJL, 714, L31
Hara, H., Watanabe, T., Harra, L. K., et al. 2008, ApJL, 678, L67
He, J.-S., Marsch, E., Curdt, W., et al. 2010, A&A, 519, A49
Hong, Z.-X., Yang, X., Wang, Y., et al. 2017, RAA, 17, 25
Ji, H., Cao, W., & Goode, P. R. 2012, ApJL, 750, L25
Kamio, S., Peter, H., Curdt, W., & Solanki, S. K. 2011, A&A, 532, A96
Lagg, A., Woch, J., Solanki, S. K., & Krupp, N. 2006, A&A, 462, 1147
Lemen, J. R., Title, A. M., Akin, D. J., et al. 2011, SoPh, 275, 17
Manrique, S. J. G., Kuckein, C., Collados, M., et al. 2018, A&A, 617, A55
Martínez-Sykora, J., Pontieu, B. D., Hansteen, V., & McIntosh, S. W. 2011, ApJ, 732, 84
McIntosh, S. W., & Pontieu, B. D. 2009, ApJL, 706, L80
McIntosh, S. W., Tian, H., Sechler, M., & Pontieu, B. D. 2012, ApJ, 749, 60
November, L. J., & Simon, G. W. 1988, ApJ, 333, 427
Parenti, S., & Vial, J.-C. 2013, in IAU Symp. 300, Nature of Prominences and Their Role in Space Weather, ed. B. Schmieder, J.-M. Malherbe, & S. T. Wu (Cambridge: Cambridge Univ. Press), 69
Pneuman, G. W., & Kopp, R. A. 1978, SoPh, 57, 49
Pontieu, B. D., & McIntosh, S. W. 2010, ApJ, 722, 1013
Pontieu, B. D., McIntosh, S. W., Carlsson, M., et al. 2011, Sci, 331, 55
Reale, F. 2014, LRSP, 11, 4
Sakao, T., Kano, R., Narukage, N., et al. 2007, Sci, 318, 1585
Schou, J., Scherrer, P. H., Bush, R. I., et al. 2011, SoPh, 275, 229
Shen, Y., Liu, Y., Liu, Y. D., et al. 2015, ApJL, 814, L17
Shumko, S., Gorceix, N., Choi, S., et al. 2014, Proc. SPIE, 9148, 914835
Solanki, S. K., Lagg, A., Woch, J., Krupp, N., & Collados, M. 2003, Natur, 425, 692
Tarr, L. A., Longcope, D. W., McKenzie, D. E., & Yoshimura, K. 2014, SoPh, 289, 3331
Teriaca, L., Banerjee, D., Falchi, A., Doyle, J. G., & Madjarska, M. S. 2004, A&A, 427, 1065
Tian, H. 2017, RAA, 17, 110
Tian, H., McIntosh, S. W., & Pontieu, B. D. 2011a, ApJL, 727, L37
Tian, H., McIntosh, S. W., Pontieu, B. D., et al. 2011b, ApJ, 738, 18
Torrence, C., & Compo, G. P. 1998, BAMS, 79, 61
Tripathi, D., Mason, H. E., & Klimchuk, J. A. 2012, ApJ, 753, 37
Wang, H., Liu, R., Li, Q., et al. 2018, ApJL, 852, L18
Warren, H. P., Ugarte-Urra, I., Young, P. R., & Stenborg, G. 2011, ApJ, 727, 58
Winebarger, A., Tripathi, D., Mason, H. E., & Zanna, G. D. 2013, ApJ, 767, 107
Wöger, F., von der Lühe, O., & Reardon, K. 2008, A&A, 488, 375
Xu, Z., Lagg, A., & Solanki, S. K. 2010, A&A, 520, A77
Zanna, G. D. 2008, A&A, 481, L49
Zirker, J. B., Engvold, O., & Martin, S. F. 1998, Natur, 396, 440
Zou, P., Fang, C., Chen, P. F., et al. 2016, ApJ, 831, 123